

Anisotropic magnetism and electronic properties of the kagome metal SmV_6Sn_6

Xing Huang,¹ Zhiqiang Cui,¹ Chaoxin Huang,¹ Mengwu Huo,¹ Hui Liu,¹ Jingyuan Li,¹
Feixiang Liang,¹ Lan Chen,¹ Hualei Sun,¹ Bing Shen,¹ Yunwei Zhang,¹ and Meng Wang^{1,*}

¹Center for Neutron Science and Technology, Guangdong Provincial Key Laboratory of Magnetoelectric Physics and Devices,
School of Physics, Sun Yat-Sen University, Guangzhou, 510275, China

Kagome magnets are expected to feature emergent properties due to the interplays among geometry, magnetism, electronic correlation, and band topology. The magnetism and topological electronic states can be tuned via the rare earth engineering in $RV_6\text{Sn}_6$ kagome metals, where R is a rare earth element. Herein, we present the synthesis and characterization of SmV_6Sn_6 , a metal with two-dimensional kagome nets of vanadium and frustrated triangular Sm lattice. Partial of the Sm atoms are shifted from the normal R positions by $c/2$ along the c axis. Magnetic measurements reveal obvious anisotropy, where the easy magnetic axis is within the ab plane. Electronic transports show multiband behaviors below 200 K. Density functional theory calculations find that the electronic structure of SmV_6Sn_6 hosts flat bands, Dirac cone, and saddle point arising from the V-3d electrons near the Fermi level. No evidence for the existence of charge density wave or magnetic order down to 2 K can be observed. Thus, SmV_6Sn_6 can be viewed as a modest disordered derivative of the $RV_6\text{Sn}_6$ structure, in which the disordered rare earth ions can suppress the magnetic order and charge density wave in the $RV_6\text{Sn}_6$ kagome family.

PACS numbers:

I. INTRODUCTION

Kagome materials RM_6X_6 (R = rare earth, M = transition metal, X = Sn, Ge) have drawn considerable attention in condensed matter physics due to their rich exotic magnetic and electronic properties¹⁻¹¹. These materials feature ideal kagome layer structures consisting of pure transition metals and naturally exhibit Dirac cone, saddle point, and flat bands that are characteristic electronic features of a kagome lattice^{1,4,12-14}. For a magnetic kagome system, such as $RMn_6\text{Sn}_6$, the magnetic structure of Mn-sublattice can be flexibly modulated by the rare earth R bearing different $4f$ moments and ion anisotropy. When R = Gd to Ho, ferrimagnetic (FIM) structures are formed, while antiferromagnetic (AFM) structures are formed when R = Er, Tm, and Lu^{3,15}. In $YMn_6\text{Sn}_6$, frustrated interplanar exchange interactions were suggested to trigger strong magnetic fluctuations, resulting in a complex magnetic phase diagram¹⁶⁻¹⁸. Of particular interest, spin-orbit-coupled kagome lattice with strong out-of-plane magnetization can achieve spin-polarized Dirac dispersion with a large Chern gap in TbMn_6Sn_6 ². The Chern-gapped Dirac fermions will host large Berry curvature and contribute to anomalous electronic and thermal transport effects^{2,19,20}. Besides, rare-earth magnetism can effectively engineer the Chern gap and related Hall conductivity³.

Compared with the robust magnetically ordered $RMn_6\text{Sn}_6$, $RV_6\text{Sn}_6$ compounds solely exhibit weak magnetic couplings among the local $4f$ moments of the R -sublattice. $RV_6\text{Sn}_6$ undergo magnetic ordering transitions at rather low temperatures. The ordering temperature is below 6 K for R = Gd-Ho, while no magnetic ordering is observed down to 1.8 K for R = Er-Yb^{5,21-26}. The crystalline electric field (CEF) of the rare earth ions is suggested to play an important role

in the development of magnetic anisotropy^{5,24}. Topologically non-trivial Dirac surface state (GdV_6Sn_6 and HoV_6Sn_6)^{1,22,27}, quantum oscillation (YV_6Sn_6)²², quantum critical behavior (YbV_6Sn_6)²⁵, and charge density wave (CDW) (ScV_6Sn_6)^{14,28,29} have been realized in the $RV_6\text{Sn}_6$ system. These results suggest that the R sublattice plays an important role in tuning the magnetic and electronic properties of $RV_6\text{Sn}_6$, driving us to explore the R -site substitution. RM_6X_6 with light R may stabilize differently crystal and magnetic structures. For example, SmMn_6Sn_6 and SmFe_6Sn_6 show the HoFe_6Sn_6 and YCo_6Ge_6 -type structures, respectively³⁰. Furthermore, SmMn_6Sn_6 displays ferromagnetism and large intrinsic anomalous Hall effect³¹.

In this work, we report the crystal growth, structure, magnetism, electronic transport properties, and band structure calculations of a newly discovered kagome metal SmV_6Sn_6 . Differing from the HfFe_6Ge_6 -type structure of $RV_6\text{Sn}_6$ (R = Gd-Lu, Y, Sc), SmV_6Sn_6 crystallizes in the hexagonal SmMn_6Sn_6 prototype³². No evidence for magnetic order and CDW can be observed above 2 K, which may be ascribed to the structural disorders of Sm. As a result of the CEF effect, the easy magnetization direction lies within the ab plane. Electronic transport measurements reveal multiband behaviors arising from the electronic bands of the vanadium kagome sublattice. Density functional theory (DFT) calculations reveal flat bands, Dirac cones, and saddle points for the kagome V-3d bands. The results highlight the interplay between the structural geometry, magnetism, and electronic correlations.

II. EXPERIMENTAL AND CALCULATION DETAILS

Single crystals of SmV_6Sn_6 were grown by the flux method²². The starting elements with a molar ratio of $\text{Sm} : \text{V} : \text{Sn} = 1 : 6 : 40$ were loaded in an alumina crucible and sealed in an evacuated silica ampoule. The ampoule was heated to 1100°C and held for 1 day, then cooled slowly at $3^\circ\text{C}/\text{h}$ to 650°C . The ampoule was taken out and loaded into a centrifuge quickly to separate the excess Sn flux. A dilute HCl solution was used to remove the residual Sn from the crystal surface. The obtained single crystals have a typical size of $2 \times 1.5 \times 0.1 \text{ mm}^3$ as shown in the inset of Fig. 2(a).

Single-crystal x-ray diffraction (XRD) was conducted on a Bruker APEX-II CCD x-ray diffractometer at 150 K. Powder XRD pattern of a crushed single crystal was collected on a powder XRD diffractometer (Empyrean) at room temperature. The elemental analysis was carried out using an energy dispersive x-ray spectroscopy (EDX) (EVO, Zeiss). Magnetic and electronic transport properties were measured on a physical property measurement system (Quantum Design). The in-plane resistivity was measured using the standard four-probe method.

DFT calculations for the structural relaxation and further electronic property of SmV_6Sn_6 were performed using the Vienna *Ab initio* Simulation Package (vasp5.4.4)³³. The exchange and correlation function was described using the Perdew-Burke-Ernzerhof generalized gradient approximation³⁴. The all-electron projector augmented wave method³⁵ was adopted to describe the electron-ion interactions, treating $5s^25p^2$, $3d^34s^2$ and $5s^25p^64f^55d^16s^2$ as valence electrons for Sn, V and Sm atoms, respectively. To ensure convergence of the total energy within a precision of 1 meV per atom, the plane-wave energy cutoff was set at 500 eV, and the Monkhorst-Pack³⁶ k -point grids with a reciprocal space resolution of $2\pi \times 0.03 \text{ \AA}^{-1}$ in the Brillouin zone were selected. Structural relaxations were performed with forces converged to less than $0.001 \text{ eV \AA}^{-1}$.

III. RESULTS AND DISCUSSIONS

A. Crystal structure

Single-crystal XRD measurements reveal SmV_6Sn_6 crystallizes in the hexagonal space group $P6/mmm$ as that of the SmMn_6Sn_6 ³², as shown in Fig. 1. The ideal V-kagome layers are separated by Sm and Sn atoms. The refined structural parameters were summarized in Table I. The measured structure factors are in good agreement with the calculated structure factors as shown in the inset of Fig. 2(a).

The results yield 22% of the Sm ions occupying on the intermediate lattice positions ($1b$ site) that are shifted from the Sm positions ($1a$) by $c/2$ along the c axis. The Sm ions on the intermediate sites enforce the nearest

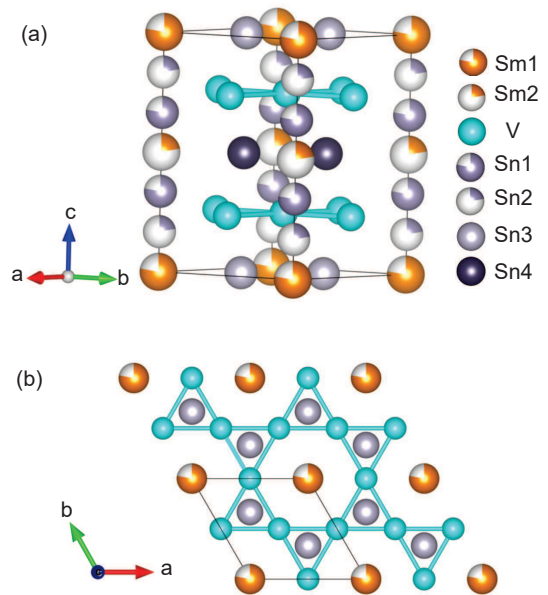


FIG. 1: (a) Three-dimensional crystal structure of SmV_6Sn_6 . The atom balls with different colors suggest that atoms have fractional occupancy. (b) Top view of the crystal structure, showing the kagome lattice consisting of V atoms.

neighbor Sn ions to the Sn2 sites. The occupancy of Sm in both the Sm1 ($1a$ site) and Sm2 ($1b$ site) positions is confirmed by the weaker intensity of the (003) reflection compared with the fully ordered GdV_6Sn_6 and HoV_6Sn_6 , as shown in Fig. 2(a)¹. The shift of the R atoms has also been observed in the other $RM_6\text{Sn}_6$ systems, where R are light rare earth elements^{30,32}. Following the lanthanide contraction rule, the lattice constants a and c in SmV_6Sn_6 are larger than that of the heavy rare earth elements, indicating the Sm ions are trivalent⁵. Thus, SmV_6Sn_6 can be regarded as a modest disordered derivative of the $RV_6\text{Sn}_6$ ($R = \text{Gd-Lu, Y, Sc}$) structure. The powder XRD pattern in Fig. 2(b) further confirms that no impurity could be identified within our instrumental resolution. Besides, the EDX measurements yield an atomic ratio of $\text{Sm} : \text{V} : \text{Sn} = 1 : 6.79 : 6.62$, close to the stoichiometry of SmV_6Sn_6 .

B. Magnetic properties

Figures 3(a) and 3(b) show magnetic susceptibility [$\chi(T)$] measured with a 0.6 T magnetic field. No obvious furcation exists between zero-field-cooling (ZFC) and field-cooling (FC) susceptibility curves. The $\chi(T)$ along the ab -plane is larger than that along the c -axis at low temperatures, revealing a strong easy-plane anisotropy. The FC susceptibility ($25 \leq T \leq 300 \text{ K}$) follows the expression: $\chi = C/(T - \theta_{CW}) + \chi_{VV}$, where θ_{CW} is the Curie-Weiss temperature, C is the Curie constant, and χ_{VV} is the temperature-independent Van Vleck

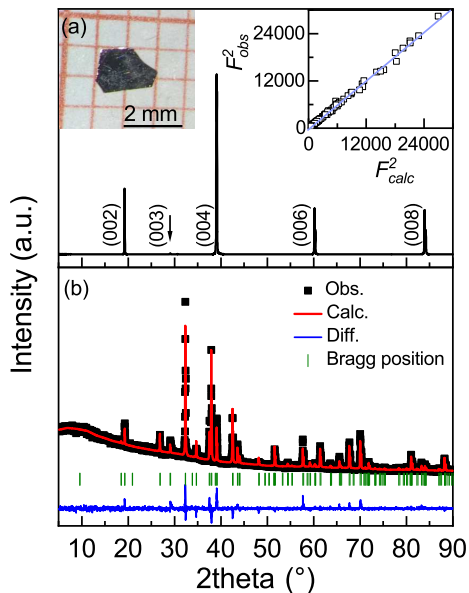


FIG. 2: (a) XRD measurement on the *ab* plane of a single crystal of SmV₆Sn₆. The inset on the left is a picture of the single crystal and the right inset shows the refinement of single-crystal diffraction. (b) A pattern of XRD measured on powder samples.

TABLE I: Crystal parameters of SmV₆Sn₆ from the single-crystal XRD at 150 K (Ga K α , $\lambda = 1.34138$ Å)

Formula	SmV ₆ Sn ₆	occupancy
Space group	<i>P6/mmm</i>	
a/Å	5.5243(6)	
c/Å	9.188(2)	
Sm1	1a(0, 0, 0)	0.78
Sm2	1b(0, 0, 1/2)	0.22
V	6i(0, 0, 1/4)	1
Sn1	2e(0, 0, 0.3356(2))	0.78
Sn2	2e(0, 0, 0.1673(9))	0.22
Sn3	2c(1/3, 2/3, 0)	1
Sn4	2d(1/3, 2/3, 1/2)	1
Goodness-of-fit on F^2	1.112	
R_1, wR_2 (all data)	0.0378, 0.0747	

contribution³⁷. Our fitting yields $\theta_{CW}^{ab} = 8.1(5)$ K, $C^{ab} = 3.99(9) \times 10^{-2}$ emu K mol⁻¹ Oe⁻¹, and $\chi_{VV} = 4.52(7) \times 10^{-4}$ emu mol⁻¹ Oe⁻¹ for $H \parallel ab$ plane; $\theta_{CW}^c = -6.1(8)$ K, $C^c = 3.86(9) \times 10^{-2}$ emu K mol⁻¹ Oe⁻¹, and $\chi_{VV} = 7.56(5) \times 10^{-4}$ emu mol⁻¹ Oe⁻¹ for $H \parallel c$ axis. The positive θ_{CW}^{ab} suggests dominant FM-type in-plane magnetic interaction while the negative θ_{CW}^c shows AFM-type out-of-plane interactions. The effective magnetic moments of Sm³⁺ ions are calculated to be $\mu_{eff}^{ab} = 0.565(1) \mu_B$ and $\mu_{eff}^c = 0.556(1) \mu_B$, which are smaller than $0.845 \mu_B$ of a free Sm³⁺ ion ($J = 5/2$, $g = 2/7$). The reduced effective moments are also observed in the other samar-

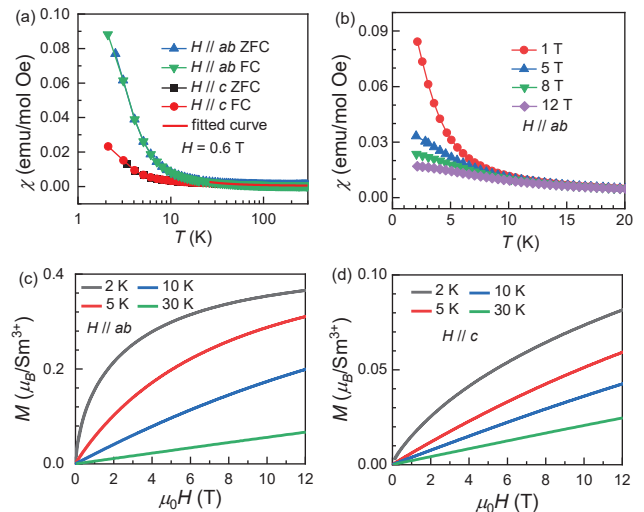


FIG. 3: (a) Temperature dependence of magnetic susceptibilities measured with a 0.6 T magnetic field along the *c* axis and *ab* plane of SmV₆Sn₆. (b) Magnetic susceptibilities measured with various magnetic fields along the *ab* plane. (c) Magnetization against magnetic fields along the *c* axis and (d) the *ab* plane at 2, 5, 10, and 30 K.

ium compounds such as Sm₃Sb₃Zn₂O₁₄ ($0.53 \mu_B$)³⁸ and Sm₂Zr₂O₇ ($0.5 \mu_B$)³⁹, which are likely related to the narrow J multiplet width arising from the large crystal field splitting of the lowest $J = 5/2$ multiplets. The magnetic susceptibility increases rapidly and large anisotropy is developed below 10 K, consistent with the development of short-range magnetic order. No evidence for a magnetic ordering transition appears down to 2 K from susceptibility measured under in-plane magnetic fields, as shown in Fig. 3(b).

Isothermal magnetization data at different temperatures are plotted in Figs. 3(c) and 3(d). Large magnetic anisotropy can be observed at low temperatures. The magnetization for $H \parallel ab$ plane is about 4.5 times larger than that for $H \parallel c$ at 2 K. When the field parallel to the *ab* plane at 2 K, the magnetization increases linearly in the low field and then gradually approach saturation. The magnetization is up to $0.37 \mu_B$ at 12 T, which is far smaller than the theoretical value of $M_s = gJ = 0.71 \mu_B$. The magnetization increases linearly for temperatures above 10 K, suggesting that the short-range order disappears at high temperatures. The magnetic anisotropy at low temperatures could be ascribed to the CEF.

C. Transport properties

Figure 4 shows the temperature dependence of the in-plane resistivity $\rho_{xx}(T)$ at 0 and 5 T magnetic fields. The resistivity decreases with decreasing temperature, consistent with the characteristic of a metal. The resistivity in the temperature range of 10–100 K follows the Fermi liq-

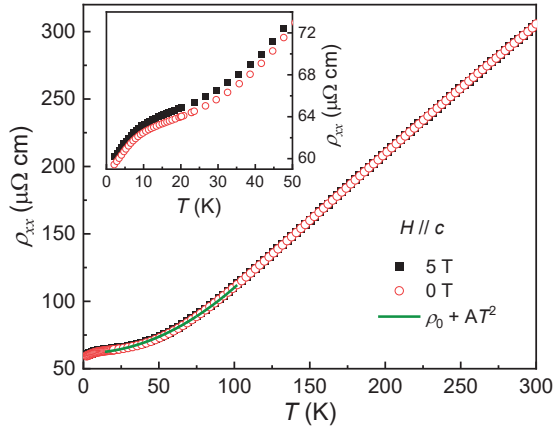


FIG. 4: Resistivity of SmV_6Sn_6 measured at 0 and 5 T magnetic fields. The green curve shows the fitting of $(\rho_{xx}(T))$ via the equation $\rho = \rho_0 + AT^2$. The inset is a zoom-in at low temperatures.

uid behavior $\rho = \rho_0 + AT^2$, giving rise to $\rho_0 = 61.58(1) \mu\Omega \text{ cm}$ and $A = 4.86(1) \times 10^{-3} \mu\Omega \text{ cm K}^{-2}$. The inset of Fig. 4 displays a decrease of resistivity below 10 K, which may be related to the formation of short-range magnetic order. In addition, the resistivity is enhanced by a 5 T magnetic field at low temperatures.

To study the magnetoresistance (MR) effect, we further measured field dependence of the longitudinal resistivity $[\rho_{xx}(H)]$ at various temperatures. The MR defined as $[\rho_{xx}(H) - \rho_{xx}(H = 0)] / \rho_{xx}(H = 0) \times 100\%$ is shown in Fig. 5(a). The current is along the ab plane and the magnetic field is along the c axis. A small magnitude of MR can be observed at all temperatures. The MR does not tend to saturate up to 12 T. The MR is gradually increased with temperature decreasing. However, a small decrease can be found at 2 K compared with that of 30 K, which may be a consequence of suppressed spin-disorder scattering.

To characterize the carrier concentrations and effective mobilities, Hall resistance $[\rho_{xy}(H)]$ measurements were performed from 2 to 300 K with the magnetic field applied parallel to the c -axis and the current within the ab plane as shown in Fig. 5(b). The $\rho_{xy}(H)$ curves are linear at temperatures $T \geq 250$ K. While the ρ_{xy} decreases nonlinearly as the temperature decreases below 250 K, signifying a multiband transport behavior. The $\rho_{xy}(H)$ curves can be fitted with a single-band model at high temperatures ($T \geq 250$ K) and a two-band model at low temperatures ($T < 250$ K). Figures 5(c) and 5(d) display the fitted results. It can be found that the concentration and mobility of the electron carriers are larger than that of the holes for most temperatures, suggesting that electrons play a dominant role in conduction. The similar multiband transport behaviors have also been observed in $R\text{V}_6\text{Sn}_6$ ($R = \text{Gd-Lu, Y}$)^{22,24,26}.

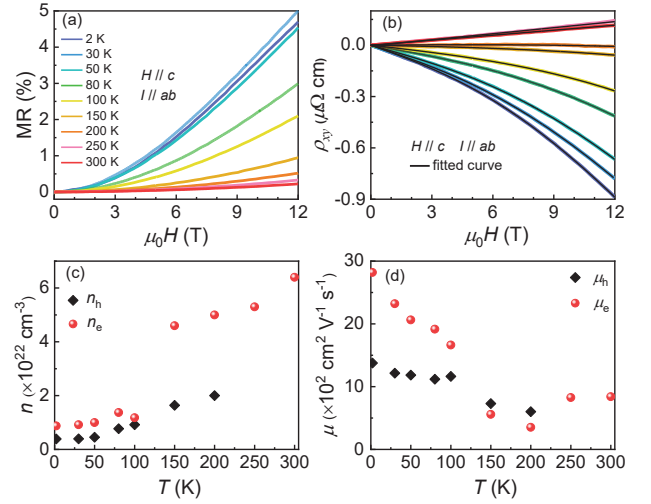


FIG. 5: (a) Magnetoresistance at various temperatures measured with $H \parallel c$ axis. The magnetoresistance component was isolated by averaging $\rho_{xx}(H)$ and $\rho_{xx}(-H)$. (b) Hall resistivity ρ_{xy} measured at different temperatures. To remove the effects of the longitudinal resistivity, ρ_{xy} is obtained via $\rho_{xy} = [\rho_{xy}(H) - \rho_{xy}(-H)]/2$. (c) Carrier densities of electrons and holes obtained from fitting of the Hall resistivity in (b) with a two-band model below 250 K and a single-band model for higher temperatures. (d) Charge carrier mobilities against temperature obtained from fitting the Hall resistivity.

D. Electronic structure

It is difficult to calculate the electronic structure via the DFT for the compound with disorders. We constructed two types of crystal structures via rearranging the atomic occupancies of the Sm and Sn sites in SmV_6Sn_6 . For the type-1 structure, the atomic occupancies of both the Sm1 and Sn1 sites are 100%; for the type-2 structure, Sm and Sn fully occupy on the Sm2 and Sn2 sites, respectively. The experimentally synthesized SmV_6Sn_6 can be regarded as an intermediate phase of the type-1 and type-2 structures. Figures 6(c)-6(f) show that the two types of structures possess similarly electronic structures, suggesting the synthesized SmV_6Sn_6 has an approximative electronic structure. The orbital projected density of states yields that the $3d$ electrons of V atoms make a dominant contribution near the Fermi level. The electronic band structures are shown in Figs. 6(e) and 6(f), an obvious kagome flat band characterized by the V d_{z^2} orbitals can be observed above E_F . Moreover, the Dirac cones and saddle points appear at the K and M points, respectively, as expected from minimal kagome tight-binding models⁴⁰. Such the transition metal-based d -orbital band structure endemic to the kagome lattice in the proximity of the Fermi level is one of the common features in the family of $R\text{M}_6\text{Sn}_6$ ^{1,4,12-14}.

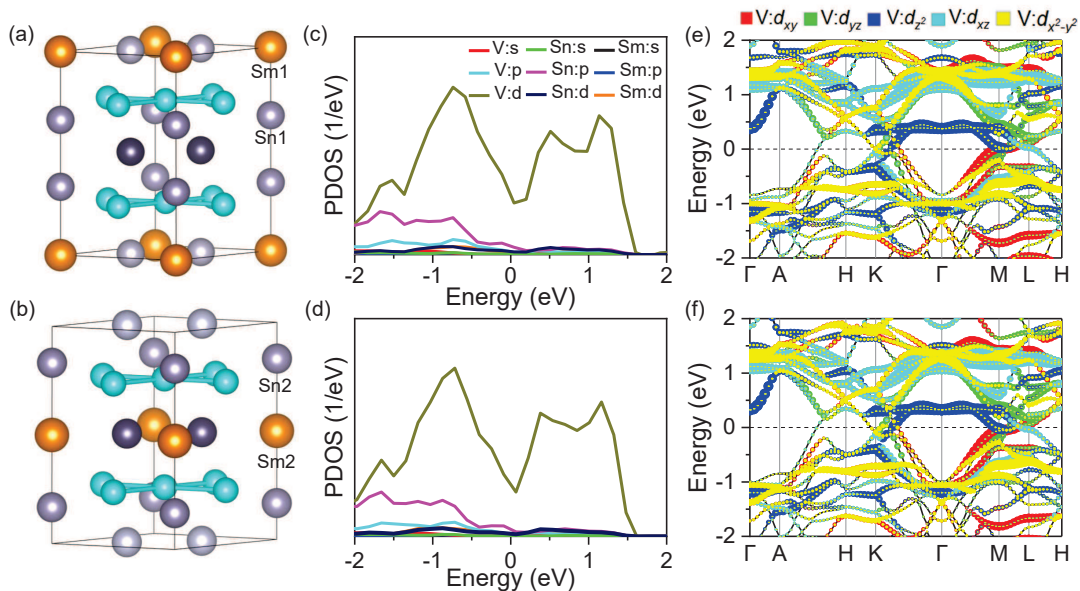


FIG. 6: (a) Sketch of the type-1 structure with fully occupied Sm1 and Sn1 sites. (b) Sketch of the type-2 structure with Sm and Sn occupying on the Sm2 and Sn2 sites. (c) Orbital projected density of states of type-1 and (d) type-2 structures. (e) and (f) $V d$ orbital decomposed band structures.

IV. DISCUSSIONS

Compared with the RM_6X_6 ($M = \text{Mn, Fe, } X = \text{Ge, Sn}$) family with magnetic ordering temperatures originated from the transition metals well above the room temperature^{6,7,11}, the moments of the rare earth ions in $RV_6\text{Sn}_6$ ($R = \text{Gd-Ho}$) order at rather low temperatures⁵. The magnetic transition temperatures of $RV_6\text{Sn}_6$ are affected by the CEF of the R ions. The leading crystal field parameter B_2^0 can be calculated via the point charge model $B_2^0 = 10(\theta_{CW}^{ab} - \theta_{CW}^c)/3(2J-1)(2J+3)$, giving rise to $B_2^0 = 1.48$ K for SmV_6Sn_6 . The positive value is close to that of TmV_6Sn_6 ⁵, which shows an easy in-plane anisotropy. Normally, a large B_2^0 with strong CEF as like -1.4 K of TbV_6Sn_6 is expected to enhance the magnetic ordering temperature⁵. However, the magnetic order has not been observed down to 2 K in SmV_6Sn_6 . The absence of magnetic order may be related to the atomic disorder associated with the shifts of the Sm^{3+} ions along the c axis.

The DFT calculations reveal that the flat bands at Γ point of the type-1 and type-2 structures locate at 0.376 and 0.326 eV, respectively. The difference should be associated with the strength of $V d$ - $\text{Sn } p$ orbital hybridization. The different V - $\text{Sn}1$ (2.872(1) Å) and V - $\text{Sn}2$ (2.865(3) Å) bond lengths will result in different strength of orbital hybridization. It was reported that ScV_6Sn_6 undergoes a CDW phase transition at 92 K, in which the V - Sn bond length is 2.822(1) Å²⁸. While no evidence of CDW is observed in the isostructural $RV_6\text{Sn}_6$ compounds with the larger ions $R = \text{Y, Sm-Lu}$ ^{5,25}. The V - Sn bond length in the $RV_6\text{Sn}_6$ family depends on the

chemical pressure arising from the rare earth ions R^{3+} . The smaller the ion radius of R^{3+} , the shorter the bond length. Thus, further explorations for smaller R systems or the effect of pressure are interesting for investigations of the interplays among lattice, charge, and magnetism.

V. CONCLUSIONS

The single crystals of the kagome metal SmV_6Sn_6 have been grown by the self-flux method. The crystal structure of SmV_6Sn_6 belongs to the SmMn_6Sn_6 prototype, showing partial crystallographic disorder associated with the appearance of the additional Sm site. Large magnetic anisotropy due to the CEF effects is found for the magnetic Sm^{3+} ions. Moments tend to align in the ab plane. No abnormal transition related to long-range magnetic ordering and CDW can be observed down to 2 K. Electronic transport measurements exhibit multiband behaviors and positive magnetoresistance properties. DFT calculations show a V - $3d$ kagome band structure near the Fermi level with a flat band, Dirac cones, and saddle points.

VI. ACKNOWLEDGMENTS

Work was supported by the Guangdong Basic and Applied Basic Research Foundation (Grants No. 2021B1515120015, 2022A1515010035), the National Natural Science Foundation of China (Grants No. 12174454,

U213010013), the Guangzhou Basic and Applied Basic Research Foundation (Grants No. 202201011123, 202201011798), Guangdong Provincial Key Laboratory of Magnetoelectric Physics and Devices (Grant

No. 2022B1212010008), and National Key Research and Development Program of China (Grant No. 2019YFA0705702).

-
- * Electronic address: wangmeng5@mail.sysu.edu.cn
- ¹ S. Peng, Y. Han, G. Pokharel, J. Shen, Z. Li, M. Hashimoto, D. Lu, B. R. Ortiz, Y. Luo, H. Li, et al., *Phys. Rev. Lett.* **127**, 266401 (2021).
 - ² J.-X. Yin, W. Ma, T. A. Cochran, X. Xu, S. S. Zhang, H.-J. Tien, N. Shumiya, G. Cheng, K. Jiang, B. Lian, et al., *Nature (London)* **583**, 533 (2020).
 - ³ W. Ma, X. Xu, J.-X. Yin, H. Yang, H. Zhou, Z.-J. Cheng, Y. Huang, Z. Qu, F. Wang, M. Z. Hasan, et al., *Phys. Rev. Lett.* **126**, 246602 (2021).
 - ⁴ M. Li, Q. Wang, G. Wang, Z. Yuan, W. Song, R. Lou, Z. Liu, Y. Huang, Z. Liu, H. Lei, et al., *Nat. Commun.* **12**, 1 (2021).
 - ⁵ L. Jeonghun and M. Eundeok, *Phys. Rev. Mater.* **6**, 083401 (2022).
 - ⁶ G. Venturini, R. Welter, and B. Malaman, *J. Alloys Compd.* **185**, 99 (1992).
 - ⁷ G. Venturini, B. C. El Idrissi, and B. Malaman, *J. Magn. Magn. Mater.* **94**, 35 (1991).
 - ⁸ X. Teng, L. Chen, F. Ye, E. Rosenberg, Z. Liu, J.-X. Yin, Y.-X. Jiang, J. S. Oh, M. Z. Hasan, K. J. Neubauer, et al., *Nature (London)* **609**, 490 (2022).
 - ⁹ P. Schobinger-Papamantellos, J. Rodríguez-Carvajal, and K. Buschow, *J. Alloys Compd.* **256**, 92 (1997).
 - ¹⁰ A. Szytuła, E. Wawrzyńska, and A. Zygmunt, *J. Alloys Compd.* **366**, L16 (2004).
 - ¹¹ X.-L. Rao and J. Coey, *J. Appl. Phys.* **81**, 5181 (1997).
 - ¹² X. Gu, C. Chen, W. Wei, L. Gao, J. Liu, X. Du, D. Pei, J. Zhou, R. Xu, Z. Yin, et al., *Phys. Rev. B* **105**, 155108 (2022).
 - ¹³ P. Wang, Y. Wang, B. Zhang, Y. Li, S. Wang, Y. Wu, H. Zhu, Y. Liu, G. Zhang, D. Liu, et al., *Chin. Phys. Lett.* **37**, 087102 (2020).
 - ¹⁴ T. Hu, S. Xu, L. Yue, Q. Wu, Q. Liu, S. Zhang, R. Li, X. Zhou, J. Yuan, D. Wu, et al., arXiv:2211.03412 (2022).
 - ¹⁵ B. Wang, E. Yi, L. Li, J. Qin, B.-F. Hu, B. Shen, and M. Wang, *Phys. Rev. B* **106**, 125107 (2022).
 - ¹⁶ R. L. Dally, J. W. Lynn, N. J. Ghimire, D. Michel, P. Siegfried, and I. I. Mazin, *Phys. Rev. B* **103**, 094413 (2021).
 - ¹⁷ Q. Wang, K. J. Neubauer, C. Duan, Q. Yin, S. Fujitsu, H. Hosono, F. Ye, R. Zhang, S. Chi, K. Krycka, et al., *Phys. Rev. B* **103**, 014416 (2021).
 - ¹⁸ N. J. Ghimire, R. L. Dally, L. Poudel, D. Jones, D. Michel, N. T. Magar, M. Bleuel, M. A. McGuire, J. Jiang, J. Mitchell, et al., *Sci. Adv.* **6**, eabe2680 (2020).
 - ¹⁹ X. Xu, J.-X. Yin, W. Ma, H.-J. Tien, X.-B. Qiang, P. Reddy, H. Zhou, J. Shen, H.-Z. Lu, T.-R. Chang, et al., *Nat. Commun.* **13**, 1 (2022).
 - ²⁰ H. Zhang, J. Koo, C. Xu, M. Sretenovic, B. Yan, and X. Ke, *Nat. Commun.* **13**, 1 (2022).
 - ²¹ H. Ishikawa, T. Yajima, M. Kawamura, H. Mitamura, and K. Kindo, *J. Phys. Soc. Jpn.* **90**, 124704 (2021).
 - ²² G. Pokharel, S. M. Teicher, B. R. Ortiz, P. M. Sarte, G. Wu, S. Peng, J. He, R. Seshadri, and S. D. Wilson, *Phys. Rev. B* **104**, 235139 (2021).
 - ²³ E. Rosenberg, J. M. DeStefano, Y. Guo, J. S. Oh, M. Hashimoto, D. Lu, R. J. Birgeneau, Y. Lee, L. Ke, M. Yi, et al., arXiv:2205.14802 (2022).
 - ²⁴ X. Zhang, Z. Liu, Q. Cui, Q. Guo, N. Wang, L. Shi, H. Zhang, W. Wang, X. Dong, J. Sun, et al., *Phys. Rev. Mater.* **6**, 105001 (2022).
 - ²⁵ K. Guo, J. Ye, S. Guan, and S. Jia, arXiv:2210.12117 (2022).
 - ²⁶ P. Ganesh, O. Brenden, C. Juan, S. Paul, K. Linus, W. Guang, R. Jacob, D. W. Stephen, et al., *Phys. Rev. Mater.* **6**, 104202 (2022).
 - ²⁷ Y. Hu, X. Wu, Y. Yang, S. Gao, N. C. Plumb, A. P. Schnyder, W. Xie, J. Ma, and M. Shi, arXiv:2205.15927 (2022).
 - ²⁸ H. W. S. Arachchige, W. R. Meier, M. Marshall, T. Matsuoka, R. Xue, M. A. McGuire, R. P. Hermann, H. Cao, D. Mandrus, et al., *Phys. Rev. Lett.* **129**, 216402 (2022).
 - ²⁹ X. Zhang, J. Hou, W. Xia, Z. Xu, P. Yang, A. Wang, Z. Liu, J. Shen, H. Zhang, X. Dong, et al., *Materials* **15**, 7372 (2022).
 - ³⁰ J. S.-Damm, E. Galdecka, O. Bodak, and B. Belan, *J. Alloys Compd.* **298**, 26 (2000).
 - ³¹ W. Ma, X. Xu, Z. Wang, H. Zhou, M. Marshall, Z. Qu, W. Xie, S. Jia, et al., *Phys. Rev. B* **103**, 235109 (2021).
 - ³² B. Malaman, G. Venturini, B. C. El Idrissi, and E. Ressouche, *J. Alloys Compd.* **252**, 41 (1997).
 - ³³ G. Kresse and J. Furthmüller, *Comp. Mater. Sci.* **6**, 15 (1996).
 - ³⁴ J. Perdew, E. McMullen, and A. Zunger, *Phys. Rev. A* **23**, 2785 (1981).
 - ³⁵ G. Kresse and D. Joubert, *Phys. Rev. B* **59**, 1758 (1999).
 - ³⁶ H. J. Monkhorst and J. D. Pack, *Phys. Rev. B* **13**, 5188 (1976).
 - ³⁷ J. Hodges, P. Bonville, A. Forget, M. Rams, K. Królas, and G. Dhalenne, *J. Phys.: Condens. Matter* **13**, 9301 (2001).
 - ³⁸ M. B. Sanders, M. B. Sander, and R. J. Cava, *J. Mater. Chem. C* **4**, 541 (2016).
 - ³⁹ S. Singh, S. Saha, S. Dhar, R. Suryanarayanan, A. Sood, and A. Revcolevschi, *Phys. Rev. B* **77**, 054408 (2008).
 - ⁴⁰ J.-X. Yin, B. Lian, and M. Z. Hasan, *Nature (London)* **612**, 647 (2022).